Chapter 3

Synthesis and Characterisation of La_2NiO_4

Part of this chapter is published as '**Katheriya, Tarun**, and Shail Upadhyay. "High temperature study of dielectric and electrical conduction behaviour of La_2NiO_4." *Physica Scripta* 98.10 (2023): 105969.'

3.1 Introduction

In the past decade, materials with a negative dielectric constant (NDC) have received a lot of attention because of their applications in electromagnetic shielding, transistors, antennas, inductor design, capacitors, and other electronic devices. It has been reported long back that below plasma frequency; the permittivity of metals has a negative sign the plasma frequency of bulk metals lies in the visible or ultraviolet band. The model to describe the negative permittivity behavior of metals was put forth by Drude in 1900[8]. This model explained the correlation of charge carrier concentration with plasma frequency. Keeping this point in view, several efforts have been made to bring down the plasma frequency from the UV band to the radio frequency band by diluting the carrier concentration of metals. Dilution of charge carrier concentration is mainly done by preparing composites of metals with polymers and ceramics. In the last decade, a significant amount of research has emerged within the realm of Negative Permittivity. Researchers have undertaken extensive investigations into the phenomenon of negative permittivity, employing diverse methodologies that vary from composite materials to single-phase materials. In 2020, a review article was published on the synthesis and dielectric characterization of polymer matrix composites and ceramic matrix composites[75]. In these composites, negative permittivity is realized only when metals are in a threshold amount or they have a critical percolating structure. Cheng et al. found strong electromagnetic shielding performance in carbon/Si_3N_4 composites because of huge impedance mismatching caused by the high negative dielectric constant values[76]. Wu et al fabricated a Graphene foam (GF/Poly): poly (styrene sulfonate) composite and investigated the electromagnetic properties in the X band region [77]. The analysis of these studies led to the conclusion that these composites have limitations for lower-dimensional applications, such as coatings or thin films because of in-homogenous composition. To overcome the challenge with composites, efforts

were made to find out systems with homogeneous composition i.e. mono-phase materials [16-18]. Negative permittivity in the radio frequency range has been reported in several undoped and doped metal [26,35] Perovskite oxides[17,21]. Among all investigated Perovskite oxides, system $La_{1-x}Sr_xMnO_3$ has been widely investigated.

La_2NiO_4 is a member of the well-researched Ruddlesden–Popper (RP) family which is commonly addressed with the general formula of $A_{n+1}B_nO_{3n+1}$. It has low thermal expansion, high mixed conductivity (electric and ionic), and high chemical stability in reducing [81,82] La_2NiO_4 has been investigated for its application as a cathode for intermediate-temperature SOFCs [83,84], ceramic permeation membrane for oxygen separation, partial oxidation of light [85,86] active catalysts for oxygen evolution in water splitting [87].

A thorough review of the literature has revealed that mono-phase materials that have exhibited negative permittivity in kHz to MHz region are transition metals based Perovskite oxides (ABO_3). To the knowledge of the authors, only a few reports are available in the literature on the investigation of the negative permittivity behavior of A_2BO_4 oxides. The structure of A_2BO_4 oxide (Ruddlesden–Popper phase with n=1) consists alternate layer of ABO_3 and AO along one of its axis. The packing fraction of this structure is lower than its counterpart ABO_3. Due to its open structure, it is easy to incorporate ions as dopants in the host lattice to influence and modify physical and chemical properties. For the first time in 2022, we observed and reported negative permittivity in one of the A_2BO_4 oxides, Sr_2MnO_4. Further, it was noted that the negative permittivity of this oxide can be tuned by incorporating a dopant at the Mn-site[35]. Crystal structure, space group, and electrical conductivity of La_2NiO_4 are similar to that of Sr_2MnO_4, these findings prompted us to study the dielectric properties of La_2NiO_4 as a function of temperature and frequency. Therefore, in this work, an attempt was

made to synthesize powder and ceramics of La_2NiO_4 and study its dielectric properties as a function of the frequency (20 Hz-2MHz) and temperature (RT-600 °C).

3.2 Experimental

3.2.1 Synthesis

In this paper, powder La_2NiO_4 was synthesized by solid-state reaction method using raw materials La_2O_3 (Alfa Assar, purity>99.9%) and $NiCO_3.2Ni(OH)_2.xH_2O$ (Sigma Aldrich, purity >99.9%). To maintain the stoichiometry of the final product La_2NiO_4, a thermal analysis of raw materials was performed. Based on the results of thermal analysis, stoichiometric amounts of raw materials were weighed and mixed in a ball mill (PM200, Retsch, Germany) for 8h at 100rpm taking acetone as a grinding media. The mixture was dried for 24 hours in a conventional oven at 80^{o}C.To fix calcination temperature, thermogravimetric (TGA) and differential scanning calorimetry (DSC) curves of the mixture of raw materials were also recorded in the temperature range of 25 - 1000 °C in N_2 atmosphere with a heating rate of 10 °C /min. The mixture was initially calcined at 1000 °C and then at 1200 °C for 12 h with an intermediate grinding step in an agate mortar. Calcined powder was mixed with 2-3 drops of 2 % polyvinyl alcohol solution and pressed into pellets of a diameter of 10mm having a thickness of about 2 mm under a hydraulic press and sintered at 1500 °C for 12 h.

3.2.2 Characterization

The phase analysis and crystal structure of calcined and sintered powders were done by X-ray diffraction (XRD) pattern over the 20 – 80^o 2θ range with $CuK_{\alpha 1}$ (1.5406 Å) radiation using an x-ray diffractometer (RigakuMiniflex II Desktop, Japan). Surface morphology studies have been carried out using Bench-top Scanning Electron Microscope (BT-SEM) instrument (Nova Nano SEM450, USA).Valence states of the constituent elements La, Ni and O were

studied by recording the core spectra of these elements employing an X-ray photoelectron spectrometer (Thermo Fisher Scientific K-Alpha, USA), operating at the high pressure of 5×10^{-11} Torr. The dielectric/electrical properties of La_2NiO_4 were measured as a function of temperature in the range of 30-600 °C and frequency in the range of 20Hz to 2MHz using an inductance- capacitance- resistance (LCR) meter (Keysight E-4980A, USA).

3.3 Result and Discussion-

3.3.1 Thermal analysis of the raw materials

It is reported that the hydration and carbonation of La_2O_3 occurs when it is exposed to the atmosphere for a longer time[88]. To confirm, we performed a thermal analysis (TGA and DSC curve) of both the raw materials La_2O_3 and $NiCO_3 \cdot 2Ni(OH)_2 \cdot 4H_2O$ using a Mettler Toledo thermal analyser. Thermo-gravimetric (TGA) and differential scanning calorimetry (DSC) curves of La_2O_3 are shown in Figure. 3.1 (a). In the TGA curve, three well-defined weight loss steps have been observed in the measured temperature range. The total weight loss in the three stages is found to be 16.6 %. The first weight loss stage observed in the temperature range of 300° C-400° C has a weight loss of ~ 10 %. This stage can be attributed to a dehydration event as given by the equation (3.1):

$$La(OH)_3 \rightarrow LaOOH + H_2O \qquad (3.1)$$

The theoretical weight loss calculated for equation. (1) is 9.48 %, close to the experimental weight loss in the first stage (10 %). The second stage weight loss (4.6%) observed in the temperature range 450° C - 550° C is due to the reaction given by equation (3.2):

$$2LaOOH \rightarrow La_2O_3 + H_2O \qquad (3.2)$$

The theoretical weight loss calculated according to equation (2) is 5.2% close to the experimentally observed weight loss in the second stage 4.6%. The third stage weight loss (2%) noted in the temperature range 650° C - 750° C may be assign to the de-carbonation as shown in equation (3.3) :

$$La_2O_2CO_3 \rightarrow La_2O_3 + CO_2 \qquad (3.3)$$

The theoretically calculated weight loss according to equation (3) is 11.89 % higher than the weight loss experimentally observed in the third stage 2 %. This difference indicates that carbonation is partial in the La_2O_3. In the DSC curve, three endothermic peaks corresponding to each weight loss stages were seen. This result confirmed that dehydration and decarbonation of La_2O_3 are endothermic in nature.

Figure 3.1(b) depicts the TGA and DSC curves of other raw material $NiCO_3 \cdot 2Ni(OH)_2 \cdot 4H_2O$. The TGA curve exhibited decomposition of this compound in two stages. The first stage weight loss observed in the temperature range RT-250°C is ~21%, which can be assigned to the removal of water molecules according to the equation (3.4):

$$NiCO_3 \cdot 2Ni(OH)_2 \cdot 4H_2O \rightarrow NiCO_3 \cdot 2Ni(OH)_2 + 4H_2O \qquad (3.4)$$

In the second stage nearly 15% of weight loss was observed at the temperature range 250°C to 350°Cthat may correspond to the expulsion of CO_2 and formation of NiO according to equation (3.5)

$$NiCO_3 \bullet 2Ni(OH)_2 \rightarrow 3NiO + CO_2 + H_2O \quad (3.5)$$

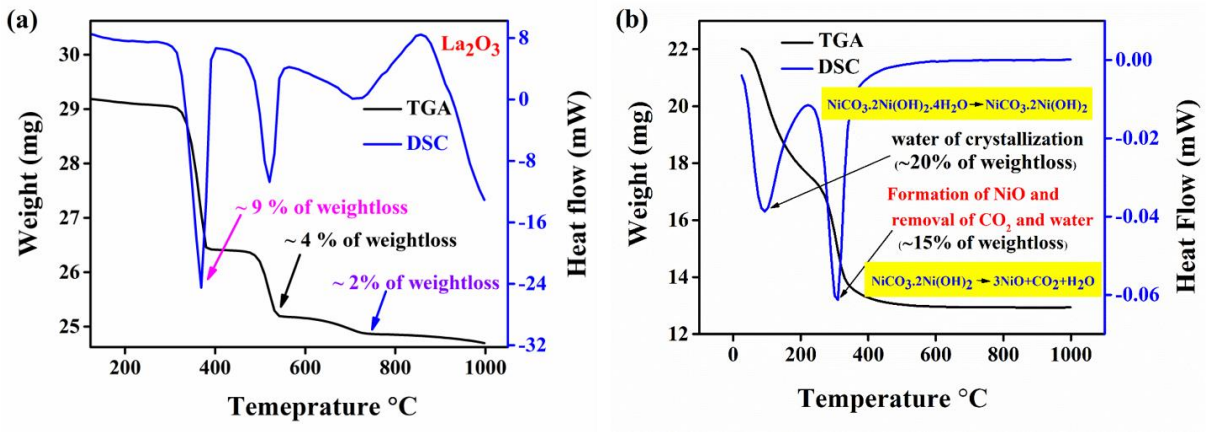

Figure 3.1.Thermal analysis of the raw materials (a) La_2O_3 (b) $NiCO_3.2Ni(OH)_2.xH_2O$.

3.3.2 Thermal analysis of the mixture of raw materials

We also recorded TGA and DSC curve of the mixture of raw materials to decide calcinations temperature. The TGA and DSC curve of the mixture is shown in Figure. 3.2. In the TGA, (Thermogravimetric Analysis) curve of the mixture, five distinct weight loss stages can be discerned, each corresponding to specific thermal events. In the initial stage, spanning from room temperature (RT) to 150°C, an initial weight loss of approximately 8% is observed. This weight loss can be attributed to the desorption of physically adsorbed water molecules on the surface of the particles or due to incomplete drying of the mixing media. Moving onto the second stage, in the temperature range of 200°C to 330°C, a weight loss of around 6% is noted. This weight loss primarily arises from the formation of Nickel Oxide (NiO), along with the accompanying liberation of water molecules, as governed by Equation 3.5. Transitioning to the third stage occurring at the temperature 300 °C – 400 °C, weight loss of approximately 6% continues to be observed. This weight reduction can be attributed to the dehydration process

whereby $La(OH)_3$ transforms into La_2O_3, a consequence of prolonged exposure to the surrounding atmosphere. In the fourth and final stage, occurring at temperatures above 500 °C up to 750 °C, a significant weight loss of approximately 12% is identified. This weight loss can predominantly be ascribed to the de-carbonization of La_2O_3 from $La_2O_2CO_3$. Above 800 ^oC no change in the weight was observed in the TGA curve of the mixture. Therefore, we decided to fix 1000 ^oC as the lowest calcination temperature. The temperature range and value of weight loss (in %) in each step for raw materials and mixture of raw materials is summarized in Table 3.1.

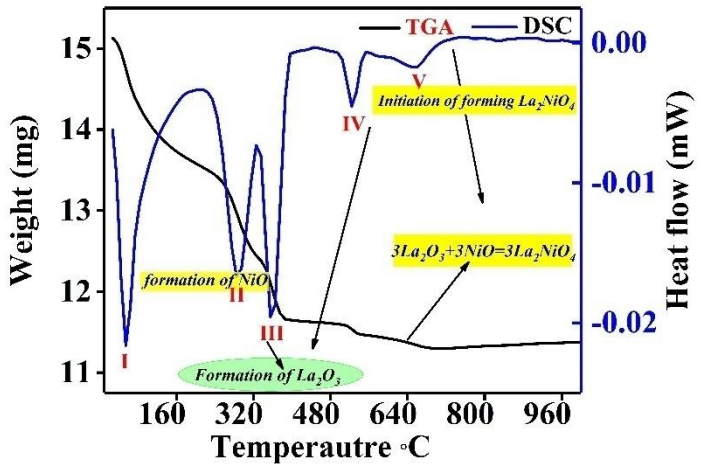

Figure 3.2 Thermal analysis of the mixture of the raw materials (La_2O_3) and $NiCO_3•2Ni(OH)_2•4H_2O$ prepared using ball-mill.

The formation of La_2NiO_4 is believed to follow a reaction mechanism, as depicted in equation (3.6).

$$3La_2O_3 + 3NiO \rightarrow 3La_2NiO_4 \qquad (3.6)$$

This process proceeds with intermediate formation of NiO around 350°C and La_2O_3, which was derived from $La(OH)_3$ and $La_2O_2CO_3$ at approximately 400°C to 650°C. Subsequently, these intermediates compound reacts at elevated temperature resulting in the formation of La_2NiO_4.

Table 3.1 Details of the weight loss stages observed in the raw materials and mixture of raw materials.

Material		Weight loss stages				
		I	**II**	**III**	**IV**	**V**
Mixture of raw materials	Weight loss (in %)	8.1	6.1	6.0	10.0	2.0
	Temperature range (^oC)	RT-150	200-330	340-400	500-550	610-700
La_2O_3	% weight loss	-----	------	10	4.6	2
	Temperature range (^oC)	------	--------	300-400	450-550	650-750
$NiCO_3•2Ni(OH)_2•4H_2O$	% weight loss	22	15	-----	-------	----- --
	Temperature range (^oC)	RT-150	250-320	------	-------	----- -

3.3.3 Phase formation and crystal structure analysis

Considering the results obtained from the thermal analysis (TGA-DSC) of the raw material & mixture, the mixture was subjected to calcination twice for 12 h, firstly at 1000°C and secondly at 1200°C. Phase formation and crystal structure were investigated using the X-ray diffraction method. The XRD pattern of the powder calcined at 1200^{o}C is shown in Figure 3.3 (a). The

peaks were matched with the crystallographic open card (COD) 1533571 for La_2NiO_4 reported in the literature[89]. Aside from the La_2NiO_4 peaks, there are a few peaks of secondary phase $LaNiO_3$ (at 31.97°) and raw material La_2O_3 (at 37°, 39°, and 62°) in the pattern. However, the intensities of the peaks of $LaNiO_3$ and La_2O_3 are weak in comparison to the intensities of the parent phase La_2NiO_4. Pellets made from the calcined powder were sintered at 1500°C for 12 h to eliminate the impurity phases and formation of a single phase of La_2NiO_4. The x-ray diffraction pattern of the sintered powder is shown in Figure 3.3(b). On matching with the aforementioned COD file, it was found that all the peaks present in the pattern belong to the La_2NiO_4 phase, and peaks of secondary phase $LaNiO_3$ and La_2O_3 have disappeared due to the formation of the desired phase as per equation (3.7).

$$2LaNiO_3 + La_2O_3 \rightarrow 2La_2NiO_4 + \frac{1}{2}O_2 \qquad (3.7)$$

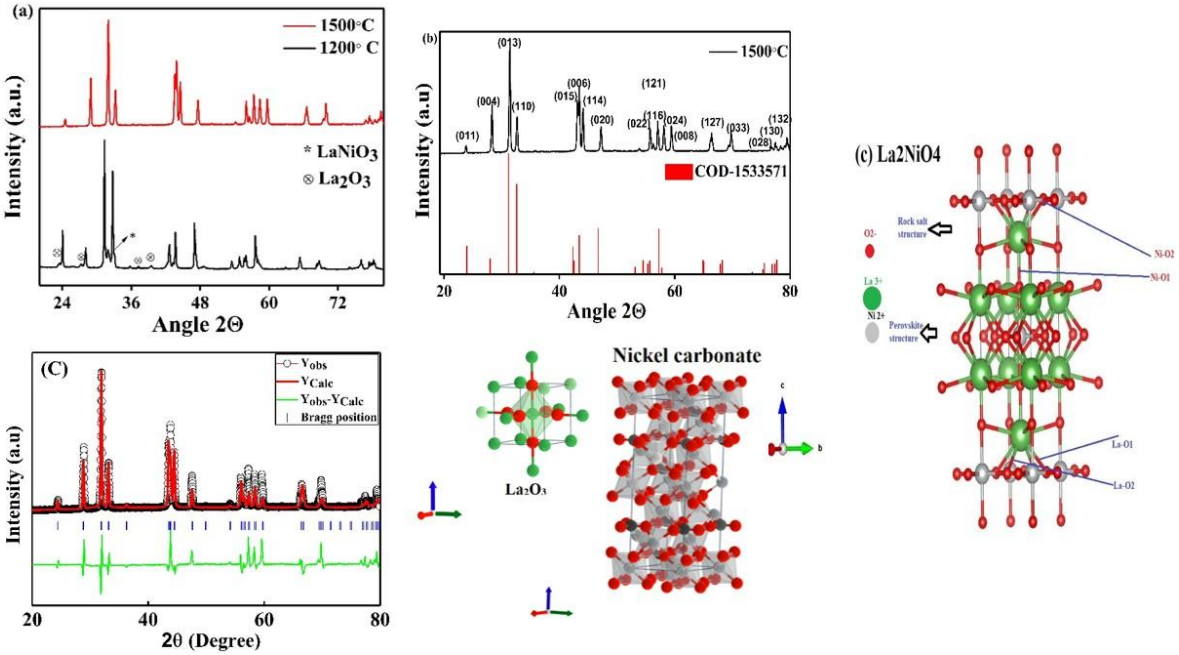

Figure 3.3 Room temperature X-ray diffraction pattern (a) calcined powder (b) sintered powder and (c) Rietveld refinement of sintered sample, 3D crystal structures of the La_2NiO_4 and raw materials.

To compute structural parameters, 'Full-Profsuite software' was used to analyze the X-ray diffraction patterns by the Rietveld refinement method. In order to characterize the peak shape, the pseudo-Voigt function was used, while the background is represented via interpolation between a collection of background points up to refinable heights. During the refinement process, the angles (α, β, γ), scale factor, background, half-width parameters, zero correction, lattice parameters (a, b, c), thermal parameters (B) positional coordinate (x, y, z) were varied, while the occupancy parameters for all ions remained constant. The refinement was carried out by considering La_2NiO_4 having a crystal structure as tetragonal and the space group (I4/mmm). In this model, La atoms are located at the 4e (0, 0, z) site, Ni at 2a (0, 0, 0) in the center of NiO_6 octahedra, and O1 at 4c (0.5, 0, 0) & O2 (0, 0.5, 0) position, respectively. The refinement leads to good agreement between the calculated and experimental diffraction patterns are shown in Figure 3.3 (c). The structural variables obtained after refinement are given in Table 3.2 which are in a good agreement with the values reported by M Saleem *et al.*[89]. The crystal structure in 3D view of the raw materials and La_2NiO_4 are also shown in the same figure.

Table 3.2 Structural parameters obtained by the Rietveld refinement of La_2NiO_4.

Sample		**Lattice parameters (Å)**
La_2NiO_4		a=b=3.867, c=12.673
Bond length (Å)	Ni-O1	1.936
	Ni-O2	2.309
	La-O1	2.582
	La-O(2a)	2.27
	La-O(2b)	2.829
Volume ($Å^3$)		181.002
Density (g/cm^3)		6.57

3.3.4 Morphological studies

Microstructure and hence surface morphology of sintered pellets have been studied employing a bench-top scanning electron microscope (BT-SEM). The micrograph of fractured surfaces of the sample La_2NiO_4 at 10,000 magnifications is displayed in Figure 3.4(a). Well-grown grains of agglomerated nature are clearly visible, grains have cuboidal shapes. SEM image clearly shows the presence noticeable amount of porosity. The presence of porosity even after sintering at 1500 ^oC requires concern about the mechanism of sintering. We know that the unit cell of A_2BO_4 oxides has one dimension (along which layering of Perovskite and rock salt takes place)

longer than the remaining two dimensions. Due to the structural diversity, these materials may exhibit an anisotropic thermal expansion of the lattice with stronger dilation along the axis C in the case of La_2NiO_4. Hence, during sintering (thermal cycling) grain growth combined with anisotropic change may lead to micro-pores [84]. The Image J software package was used to generate a histogram of the grain size distribution in the micrograph. Figure 3.4(b) shows the average grain size after fitting the Gaussian function to these histograms was calculated. The average grain size is found to be 2.29 μm. The bulk density of the sintered La_2NiO_4 pellet was measured using Archimedes' principle and found to be **6.77 g/cm³**, which corresponds to a **porosity of approximately 3%** relative to the theoretical density of **7.01 g/cm³**.

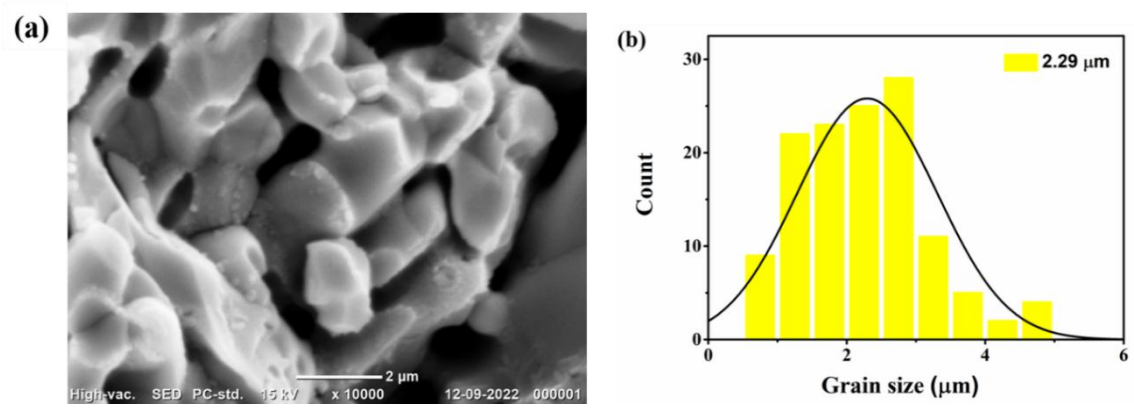

Figure 3.4 (a) SEM image of the fractured surfaces of the pellet and (b) Histogram of the distribution of grain size.

3.3.5 X-ray photoelectron spectroscopy analysis

The X-ray photoelectron spectroscopy (XPS) technique was employed to elucidate the valence states of the constituent ions (La, Ni and O). The survey scan report of La_2NiO_4 is shown in Figure **3.5(a).** It was found that peaks belong to the constituent elements La (3d) and Ni (2p) and O (1s) only. For the calibration of binding energies C1s peak observed at 285 eV was used.

The core level spectra of La (3d), Ni (2p) and O (1s) are demonstrated in Figures 3.5 (b-d). The core level peaks were fitted using the Shirley function as Voight (mixed Lorentzian- Gaussian).

The XPS spectrum of Ni $2p_{3/2}$ as shown in Figure 5(b), displayed two conspicuous peaks at 855.2 eV and 851.6 eV that could be assigned to the characteristic peak of Ni $2p_{3/2}$ and its satellite peak, respectively, indicating that the valence state of Ni is Ni^{2+} in the sample. The possibility of Ni existing in the Ni^{3+} state is ruled out because no peak above 855.2 is seen in the spectrum of Ni [90]. The core level XPS spectrum of La (3d) is shown in Figure 3.5 (c), it consists of the spin-orbit splitting of La $3d_{5/2}$ and $3d_{3/2}$. For the synthesized sample, the representative peaks of $3d_{5/2}$ are centered at 834.28 eV and 838.29 eV, and the peaks of $3d_{3/2}$ are located at 851.53 eV and 855.14 eV. On comparing with literature it is concluded that La is present in La^{3+} state [90]. The XPS spectrum of O (1s) is depicted in Figure 3.5 (d) shows a single peak having asymmetry on both the sides (lower and higher binding energy). We have de-convoluted this peak into three peaks. These peaks are assigned to adsorbed (-OH), lattice oxygen and oxygen vacancies using literature report [91]. The presence of the (-OH) group indicates the absorption of moisture on the surface of the sample during measurements. Formation of oxygen vacancies in ceramic oxides is common when they are synthesized at higher temperatures.

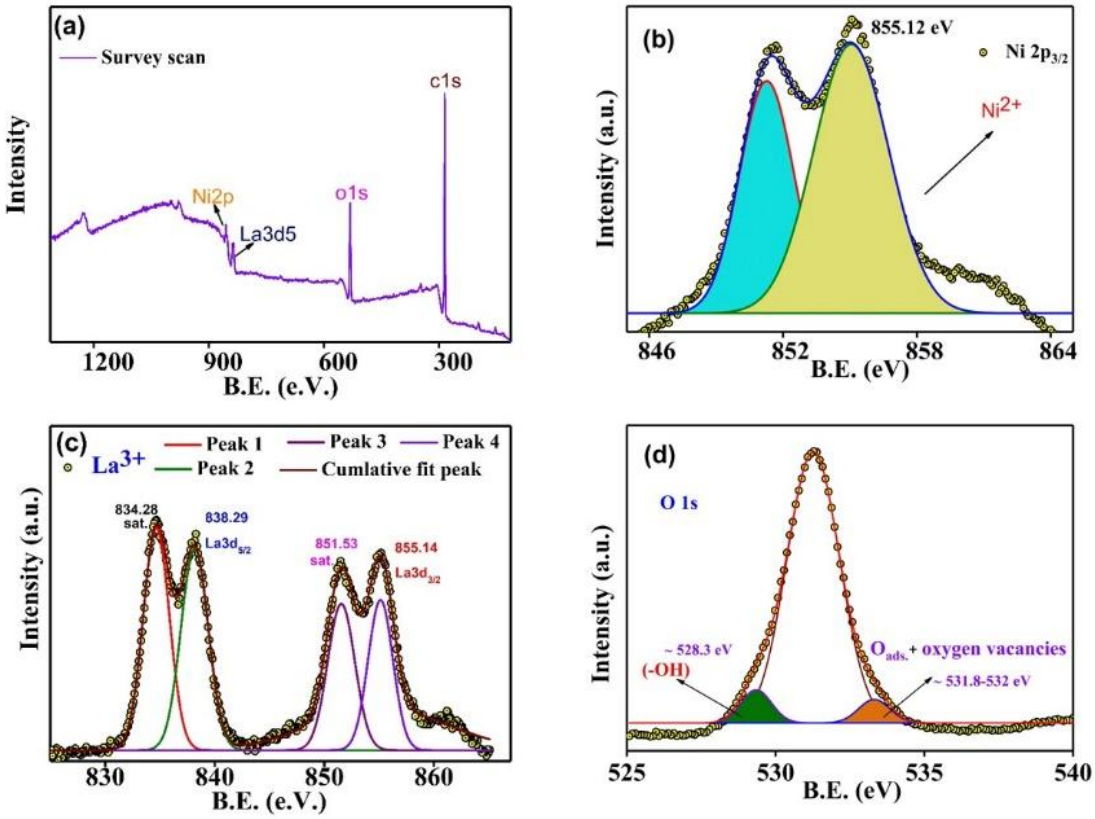

Figure 3.5 The XPS spectrum of (a) survey scan and core level of (b) Ni (c) La and (d) O.

3.4 Dielectric characterization

3.4.1 Electrical properties of the Sample holder/Electrode

Given the high conductivity of our sample, there is a risk that the properties of the sample holder could affect the material's characteristics, potentially leading to inaccurate results. To address this concern and ensure that the material properties are independent of the sample holder and electrode contributions, we implemented the following precautions:

1. **Avoided Conductive Paste:** We refrained from using any conductive paste, as it can introduce significant measurement errors.
2. **Measured Electrode Properties:** We conducted measurements of the electrical properties, including inductance (L) and resistance (R), of the electrodes and connecting wires.

3. **Data Correction:** We subtracted these measured values from the results obtained when assessing the material properties.

By following these steps, we aim to enhance the accuracy and reliability of our results. After conducting the experiment and measuring the electrode performance over the range of 30 to 600ºC, we observed that the inductance is in µH to nH range, while the resistance is less than 1 ohm shown in Figure 3.6. As shown in Figure 3.6, the resistance of the silver (Ag) electrode exhibits a typical metallic behavior, increasing with temperature. This data is taken as a reference and subsequently subtracted from the sample measurements for further analysis.

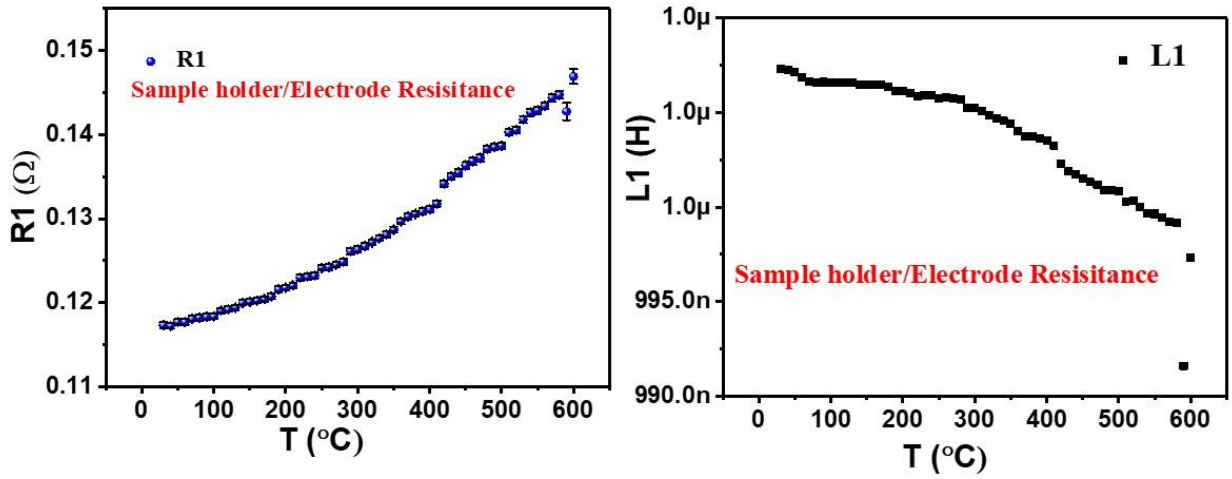

Figure 3.6 The resistance R1 (left) and inductance L1 (right) of the sample holder/electrode without inserting the pellets. It is evident from the trend that resistance R1 is increasing and inductance is decreasing on increasing the temperature, representing the pure metal characteristics.

The temperature-dependent real permittivity (ε_r') and dielectric loss (tanδ) of La_2NiO_4 have been measured at various temperatures (from 30 °C to 600 °C) in the frequency range 20 Hz - 2MHz. The variations of these quantities with the temperature at a few selected frequencies are shown in Figure 3.7. In Figure 3.7(a), negative permittivity is observed at all measured

temperatures and frequencies. Meanwhile, the absolute value of negative permittivity increases with increasing temperature up to 450°C, above 450 °C decrease in the absolute value is seen. The increment and decrement in absolute value of ε_r' decreases with increasing frequency.

The variation of dielectric loss D with frequency is shown in Figure 3.7(b), Dielectric loss, D at low frequencies (<1 kHz) increases with temperature up to 450 °C, but at higher frequencies, it becomes almost independent of temperature.

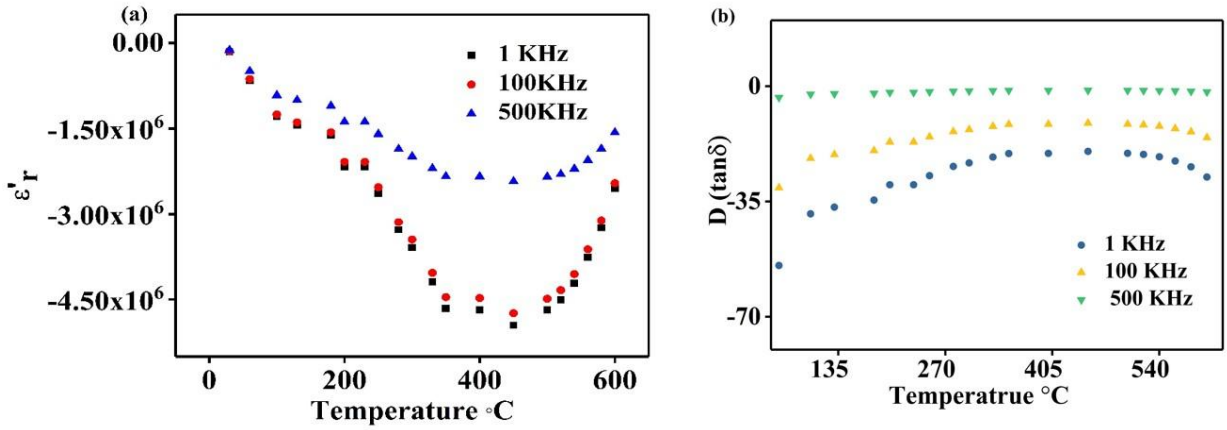

Figure 3.7 Variation of (a) relative permittivity (ε_r') and (b) dielectric loss, D with temperature at some representative frequencies.

To understand the origin of the negative permittivity in depth, real permittivity (ε_r') and dielectric loss (tanδ) are plotted as a function of frequency at a few selected temperatures, shown in Figure 3.8 (a) and (b), respectively. The magnitude of permittivity increases with increasing temperature up to 450 °C and thereafter its value decreases with increasing temperature. Meanwhile, the dispersion in ε_r' with frequency increases with increasing temperature. It is noted that at all the temperatures of measurements value of dissipation factor (D) remains negative. Its absolute value decreases sharply with increasing frequency up to 10 kHz and afterwards, it becomes constant on further increase in temperature. Its sign remains negative in the entire frequency range of measurement. Similar behaviour has been observed in other ceramic oxides as well [21,36,37].

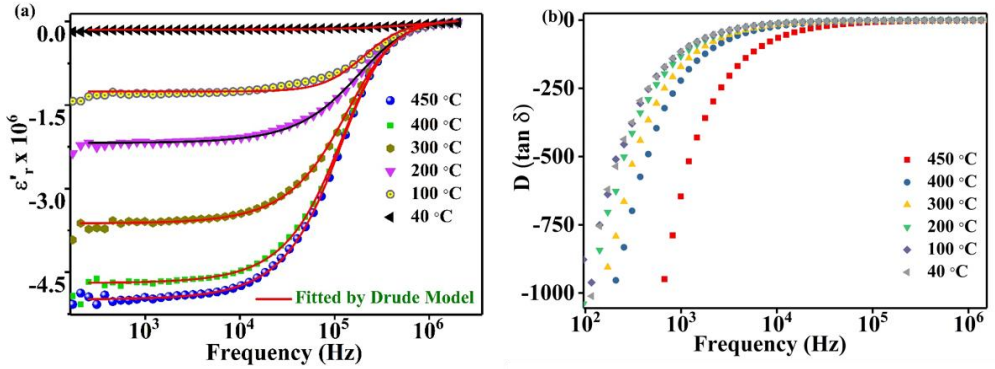

Figure 3.8 The variation of (a) relative permittivity (ε_r') and (b) dissipation factor (D) with frequencies at some representative temperature.

In the literature two theoretical models Drude and Drude-Lorentz have been applied to fit the experimentally data of the negative permittivity. Drude model has been mainly used by the researchers to explain the negative permittivity behavior of metals and semiconductors[10,38]. According to this model, the real part of complex permittivity (ε_r') is given by the equation (3.8):

$$\varepsilon_r' = 1 - \frac{\omega_p^2}{\omega_\tau^2 + \omega^2} \qquad (3.8)$$

ω_τ is the damping factor which depicts electrons collision frequency and ω_p is the Drude plasma frequency, which is related to the carrier–concentration (n_{eff}), effective mass (m*) and electronic charge (e) as given below:

$$\omega_p = \sqrt{\frac{n_{eff.}e^2}{m^*\varepsilon_0}} \qquad (3.9)$$

The Drude model (Equation. (3.8)) was fitted to the experimental data points, as shown in Figure 3.8(a). In this figure, the solid lines represent data generated by the Equation. (3.8), while the symbols represent experimental data points. A good matching between solid lines

and experimental data points suggests that negative permittivity originates due to plasma oscillation of free (delocalized) electrons as observed in metals and semiconductors. Values of ω_τ and ω_p obtained by fitting at different temperatures are presented in Table 3.3.

Table 3.3Parameters obtained by fitting the Drude model to negative permittivity.

Temperature (° C)	**ω_τ (MHz)**	**ω_p(GHz)**	**n_{eff} (m^{-3})**
100	1.51	1.32	$9.192x10^{14}$
200	1.17	1.38	$9.912\ x10^{14}$
300	0.91	1.39	$1.007\ x10^{15}$
450	0.62	1.41	$1.027\ x10^{15}$
500	0.82	1.48	$1.044\ x10^{15}$
600	1.06	1.44	$1.022x10^{15}$

The order of $\boldsymbol{\omega_\tau}$ and $\boldsymbol{\omega_p}$ presented in Table 3 is in agreement with the literature reports [95]. It is noted that $\boldsymbol{\omega_\tau}$ decreases whereas $\boldsymbol{\omega_p}$ increases with increasing temperature up to 450 ^oC**.** The decrease in the value of ω_τ suggests that La_2NiO_4 is not behaving perfectly as metals. In the case of metals ω_τ (= $1/2\pi\tau$, τ is relaxation time) increases with increasing frequency, and hence resistance increases with temperature. Increasing the value of τ with temperature suggests that the transport mechanism in the sample is different than the metals. Assuming that m^* =m, values of n_{eff} were calculated using equation (9) and shown in Table 3.3. It is noted that n_{eff} is increasing gradually with increasing temperature. The core spectrum XPS analysis of O (1s) has confirmed the presence of oxygen vacancies in the synthesized sample. To maintain charge neutrality, electrons or negative defects have to be generated inside the lattice. At low temperatures, these electrons remain trapped in the energy states of oxygen vacancies. At high

temperatures, due to the significant thermal energy weakly bonded electrons dissociate from the oxygen vacancies and behave as free electrons.

We have noted from the literature that studies on the dielectric behavior of La_2NiO_4 have been carried out mainly at low temperatures. No reports in the literature are found on the study of dielectric properties at high temperatures for comparison purposes. Although, we have checked the reproducibility of negative dielectric data of La_2NiO_4 observed at high temperatures by using different experimental set-ups available to us. However, to reconfirm that the negative permittivity behaviour is the intrinsic characteristic of La_2NiO_4, not a measurement artefact (sample holder, electrode-sample interface, etc.) we have calculated AC conductivity (σ_{ac}) in the same temperature and frequency range in which permittivity and dissipation factor were measured. The variation of σ_{ac} against frequency at selected temperatures is shown in Figure. 3.9 (a). At low frequencies (up to 100 kHz) σ_{ac} is independent of frequency, at high frequencies σ_{ac} decreases with increasing frequency which is attributed to the skin effect of conduction electrons observed particularly in metals. The tendency of an alternating electric current (AC) to become distributed within a conductor such that the current density is largest near the surface of the conductor and decreases exponentially with greater depth in the conductor is known as the Skin effect. The electric current flows mainly at the "skin" of the conductor, between the outer surface and a level called the **skin depth**. Skin depth depends on the frequency of the alternating current. As frequency increases, current flow becomes more concentrated near the surface, resulting in less skin depth. Skin effect reduces the effective cross-section of the conductor and thus increases its effective resistance leading to a reduction in AC conductivity as frequency increases.

According to Drude's model, AC conductivity of the metals varies as shown below [96]:

$$\sigma_{ac} = \sigma_{dc}\frac{\omega_\tau^2}{\omega^2 + \omega_\tau^2} \qquad (3.10)$$

By fitting Equation. (3.10) to the experimental data shown in Figure. 3.9 (a), we have obtained the value of DC conductivity (σ_{dc}) and ω_τ at various temperatures, given in Table 3.4.

Table 3.4 Parameters obtained from the Drude model fitting for AC conductivity.

Temperature (°C)	**DC conductivity σ_{dc} ($S.m^{-1}$)**	**ω_τ (MHz)**
100	15.72	1.51
200	20.32	1.17
300	26.11	0.92
450	30.85	0.67
500	29.85	0.81
600	23.69	1.01

From Table 3.4 it is observed that as temperature increase DC conductivity increases whereas ω_τ decreases up to 450 ^oC. In Tables 3.3 and 3.4, the value of ω_τ decreases or τ (relaxation time) increases with temperature, which is contradictory to the increasing trend of τ with temperature opposite as, observed in the case of metals. The increasing trend of τ with temperature may be due to "**hopping type conduction"** in the sample. An increasing trend of DC conductivity with

temperatures up to 450°C confirms the semiconducting nature of the sample. The variation of σ_{dc} with temperature is shown in Figure. 3.9 (b) it was observed that conductivity first increases with temperature and attains a maximum value around 450 ^oC afterward it started decreasing with increasing temperature. This plot clearly shows a transition in the electrical behavior from semiconductor (negative temperature coefficient of resistance) to metal (positive temperature coefficient of resistance) around 450 ^oC. Semiconductor-to-metal transition in La_2NiO_4 has been reported by earlier researchers [41, 42]. The agreement of electrical transition observed by us with earlier researchers confirms that the negative permittivity characteristic of La_2NiO_4 is its intrinsic behavior not due to measurement artefacts.

To understand the mechanism of DC conduction a plot of log σ_{dc} with 1000/T is shown in Figure. 3.9 (c). The linear increase in log σ_{dc} with the inverse of temperature shows that conductivity obeys the Arrhenius relation as given below:

$$\sigma_{dc} = Ae^{-E_a/k_\beta T} \qquad (3.11)$$

Where A represents the pre-exponential factor, E_a denotes the activation energy for DC conduction, k_β is the Boltzmann constant, and T denotes the absolute temperature in kelvins (K). In the temperature range RT- 450 ^oC, the corresponding activation energy calculated from the slope of the straight line is ***0.053 eV***, which is close to the value reported by other researchers [43]. In some literature reports, small polaron hopping mechanism in La_2NiO_4 has been reported for the similar value of the activation energy[41,43,44].

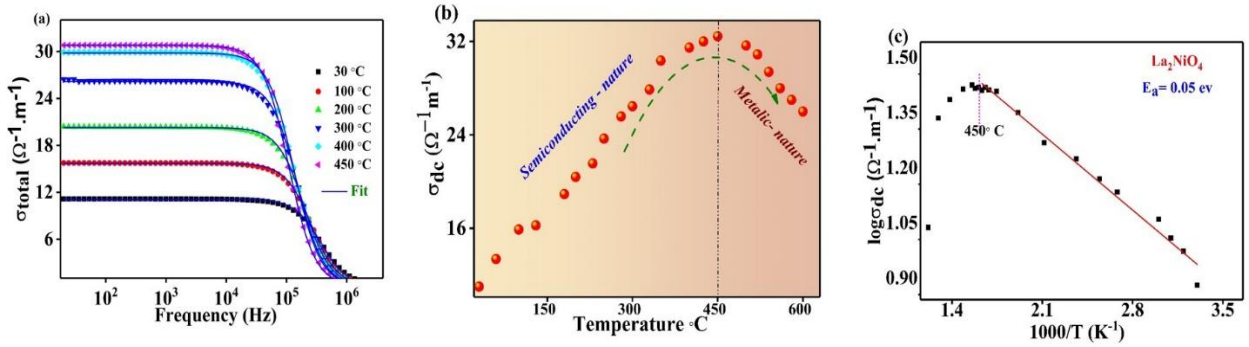

Figure 3.9 Variation of (a) AC conductivity of the sample with frequency at some representative temperatures (b) DC conductivity with temperature (c) DC conductivity with the inverse of temperature.

A comparative study of a few recently investigated materials, focusing on their observed parameters of permittivity is shown in Table (3.5).

Table 3.5 Comparison of dielectric parameters (kHz-MHz) of La_2NiO_4 with some recently investigated materials and their parameters (Highlighted materials were measured in GHz frequency range).

Sample	**Dielectric constant**	**Conductivity ($S.cm^{-1}$)**	**ω_p (Hz)**	**ω_τ (Hz)**	**T (° C)**	**Structure**	**Ref.**
La_2NiO_4	~-4.5x 10^6	3500	~10^9	~10^6	RT	R-P phase	This work
Sr_2MnO_4	~ -2 x 10^3	~1000	-	-	580	R-P phase	[35]
$Sr_2Sn_{0.3}Mn_{0.7}O_4$	~-1.2 x 10^5	~2000			240		
$Sr_2Sn_{0.5}Mn_{0.5}O4$	~-1.2 x 10^5	~1500			360		

$Sr_2Nb_{0.3}Mn_{0.7}O_4$ $Sr_2Nb_{0.4}Mn_{0.6}O_4$ $Sr_2Nb_{0.5}Mn_{0.5}O_4$	~ $-5x10^5$ ~ $-2x10^5$ ~ $-8x10^4$	~1500 ~1200 ~1000	--	--	80 180 230	R-P phase	[101]
$La_{0.86}Ba_{0.14}CoO_3$ $La_{0.9}Ba_{0.1}CoO_3$	~ $-1x10^4$ ~ $-6x10^4$	~0.01 ~0.04	--	--	RT-300	Pervoskite	[102]
$PrMnO_3$	~ -2500	--	--	-	250	Pervoskite	[103]
$La_{1-x}Sr_xMnO_3$	~ $-2x10^5$	--	~ 10^9	~10^6	--	Pervoskite	[79]
Cu-TiO_2	~$-6x10^5$	~$5x10^{-2}$	--	--		Composite	[104]
Cu-Epoxy	~ $-5x10^4$	~10^{-2}				Composite	[105]
$Sn_{0.92}Sb_{0.08}O_2$ $Sn_{0.90}Sb_{0.10}O_2$	~ -2.5x 10^5 ~ -2.0x 105	~10	~10^{10}	~10^6	--	Rutile	[95]

Graphene -polymer	~ -250	--	~ 10^{10}	~ 10^5	--	Composite	[77]
PVA-CB	-443	~$4x10^{-4}$	--	--	--	Composite	[106]
CCTO-14% Graphene CCTO-18% Graphene	~$-5x10^3$ ~$-5x10^4$	~50 ~80	~10^9	~10^8	--	Composite	[107]

As observed from Table 3.5, the magnitude of the attained negative dielectric constants and conductivity of other materials is considerably less when compared to our synthesized sample. One can say that the absolute value of the negative dielectric constant (NDC) and temperature at which negative permittivity is observed depends mainly on the conductivity of the material. Further, it is important to note that undoped and Sn/Nb-doped Sr_2MnO_4 systems exhibit NDC observed at high temperatures. However, La_2NiO_4 in undoped form exhibits negative permittivity at room temperature in the KHz frequency range. The realization of negative permittivity at room temperature has great importance in practical electronics and electromagnetic devices.

3.4.2 Reactance analysis of La_2NiO_4

It is reported that the change in the sign of permittivity from positive to negative is due to a change in the electrical characteristic from capacitor to inductor. This can be verified by complex plane impedance analysis. Complex impedance in its real and imaginary components is expressed as$Z^* *= Z' - iZ"$. The relationship between components of impedance is given by equation, (3.12):

$$\varepsilon' = -\frac{Z"}{2\Pi f C_o [(Z'^2) + (Z"^2)]} \qquad (3.12)$$

Where ε_r' is the real permittivity, f is the test frequency and C_o is the capacitance of vacuum. It is quite obvious that when the imaginary part of the impedance (Z'') has negative values, positive values of permittivity appear and when it has positive values, negative permittivity is observed. Capacitive reactance is –j/ωc and inductive reactance is iωL, indicating that the negative values of Z'' ($Z'' < 0$) represent a capacitive character, while the positive values of Z'' ($Z'' > 0$) indicate the inductive character [46]. In summary, the capacitive characteristic leads to positive permittivity, and the inductive characteristic is responsible for negative permittivity. In order to know the electrical nature of the synthesized sample, a plot between the Z' and Z'' at various temperatures in shown in Figure 3.10. One can see those values of Z'' remain positive at all temperatures and frequencies, confirming the inductive nature of the sample in the investigated range of temperature and frequency. This signifies that the negative permittivity induced by plasma oscillation can be attributed to the inductive characteristic. Ceramic-based negative permittivity materials may have higher inductance density than traditional inductors made of wire coils. As a result, ceramic materials showing negative permittivity have the potential for coil-less inductors[49,52,53].

It is noted from Figure 3.10 that the value of Z′ at the lowest frequency (intercept on the x-axis) decreases with increasing temperature up to 450 ^oC. As we know Z′ represents DC resistance, decreasing value with increasing temperature is the signature of the semiconducting behavior of the sample up to 450 ^oC. A higher value of DC resistance at 600 ^oC is due to the change in the nature of the sample from semiconductor to metal.

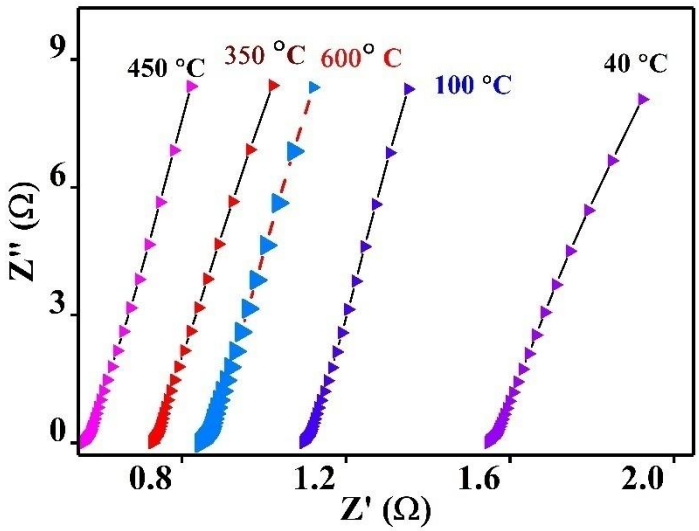

Figure 3.10 The schematic representation between Z' and Z" at few temperatures.

3.5 Conclusion

Single-phase La_2NiO_4 was successfully synthesized by solid-state reaction method. Rietveld refinement of the observed X-ray diffraction pattern confirmed that the synthesized sample of La_2NiO_4 has a tetragonal structure and the space group I4/mmm. Analysis of the SEM image has confirmed the non-uniform growth of cuboidal-shaped grains. The average grain size is found to be 2.29 μm. The real part of permittivity is found to be negative at all measured frequencies and temperatures. The Drude model fitted well to the experimental data points and negative permittivity behavior is attributed to plasma oscillation of free charge carriers. AC conductivity at high frequencies has shown the skin effect, mainly observed in metals. A change in behavior from semiconductor to metal around 450 ^oC has been observed in the

conductivity which confirms that the negative permittivity of La_2NiO_4 is its intrinsic property. The lower value of activation energy (E_a) for DC conduction indicated small polaron hopping conduction mechanism. Positive values of the imaginary part of the impedance (Z″) confirmed the inductive nature in the entire range of temperature and frequency measurement. This is the preliminary report on the negative permittivity behavior of La_2NiO_4, more measurements and in-depth analysis of the results are required to develop this system for device applications. This work has discovered a new Perovskite oxide showing negative permittivity at and above room temperature without doping. The investigated compound can be an alternative for those applications in which metal-materials/meta-composites are used.

Chapter 4

Synthesis and Characterisation of $La_{2-x}Sr_xNiO_4$

Part of this chapter '**Katheriya, Tarun**, Gurudeo Nirala, and Shail Upadhyay. "Establishing the correlation of negative permittivity and AC conductivity of $La_{2-x}Sr_x NiO_4$ (x= 0, 0.1, 0.3, 1.0) for microwave shielding applications." Journal of Materials Chemistry C 12.23 (2024): 8473-8484'.